Environmental Pollution 367 (2025) 125598

Contents lists available at ScienceDirect

Environmental Pollution

journal homepage: www.elsevier.com/locate/envpol

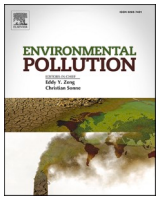

Innovative spherical Fe-Mn layered double hydroxides (LDH) for the degradation of sulfisoxazole through activated periodate: Efficacy and mechanistic insights☆

Junle Jian, Siling Zhang, Ping Chen, Dezhu Liu, Yishun Wang, Linsheng Liu, Zhenjun Xiao, Zihong Xu, Yuhang Pan, Wenying Lv *, Guoguang Liu **

Guangdong Key Laboratory of Environmental Catalysis and Health Risk Control, School of Environmental Science and Engineering, Institute of Environmental Health and Pollution Control, Guangdong University of Technology, Guangzhou, 510006, China

ARTICLE INFO

Keywords:
Layered double hydroxide (LDH)
Periodate
Sulfisoxazole
Advanced oxidation processes
Degradation mechanism

ABSTRACT

Advanced oxidation technology based on peroxides is widely regarded as an efficient method for treating emerging contaminants. However, the precise mechanism by which layered double hydroxides (LDHs) enhance oxidant activation requires further investigation. In this study, a spherical Fe-Mn LDH (S-FML) with improved crystallinity using a simple hydrothermal method. Compared to granular Fe-Mn LDH (G-FML), S-FML demonstrated superior periodate (PI) activation efficiency and outstanding stability. Intensive mechanistic studies have shown that the synergistic action of Fe^{2+} and Mn^{2+} in S-FML plays a key role in the degradation reaction. Three primary pathways for SIZ degradation and a reduction in solution toxicity post-reaction were identified through analysis of degradation intermediates and density functional theory (DFT) calculations. This research offers valuable theoretical insights and a scientific foundation for designing high-performance heterogeneous catalysts and elucidating the efficient activation mechanisms of PI for emerging pollutant treatment.

1. Introduction

In recent years, the increased production and use of pharmaceuticals and personal care products (PPCPs) have led to their emergence as critical environmental contaminants. Most of these compounds are identified as endocrine disruptive chemicals (EDCs) or potential carcinogens (Kumar et al., 2023; Yu et al., 2021). However, the conventional wastewater treatment process has a limited effect in removing PPCPs (Santos et al., 2007). Studies have reported the presence of PPCPs in wastewater treatment plants across various countries (Liu and Wong, 2013), including the United States (Boyd et al., 2004), Finland (Lindqvist et al., 2005), Spain (Carballa et al., 2004), and China (Wang et al., 2023). Among these PPCPs, sulfonamides (SAs), a widely used class of broad-spectrum antibiotics, are especially difficult to remove via conventional biological wastewater treatment due to their polar and antimicrobial properties (Liu et al., 2024b; Song et al., 2017).

Advanced oxidation processes (AOPs) are emerging as promising technologies for treating PPCPs, offering high oxidation efficiency with less secondary pollution (Kurban et al., 2024; Ni et al., 2023; Saravanan et al., 2022). These processes necessitate the utilization of solid oxidizing agents to generate active substances that facilitate the decomposition of persistent organic micropollutants. Periodate (PI) are of particular interest due to their safety and stability during transportation and storage, as well as their efficacy in water treatment.t (He et al., 2022; Zong et al., 2021). However, PI has a low redox potential (+1.6 V) (Long et al., 2021), limiting its ability to degrade organic pollutants. Research has shown that PI's oxidative properties can be activated by UV light ($\lambda < 266$ nm (Chia et al., 2004; Zhang et al., 2023), transition metals (Fang et al., 2022; Theerthagiri et al., 2022a), hydroxylamine (Sun et al., 2020), and freezing (Choi et al., 2018). Transition metal catalysts are widely regarded as the most promising catalysts due to their excellent activation performance and low price (Long et al., 2022), and the development of new transition metal catalysts that are stable (low leaching rate) and reusable is necessary (Naik et al., 2021).

The most commonly widely used transition metal catalysts are based

☆ This paper has been recommended for acceptance by Dr Hocheol Song.

* Corresponding author.
** Corresponding author.
E-mail addresses: lvwy612@163.com (W. Lv), liugg615@163.com (G. Liu).

https://doi.org/10.1016/j.envpol.2024.125598
Received 15 November 2024; Received in revised form 22 December 2024; Accepted 26 December 2024
Available online 26 December 2024

on Co-, Fe-, Mn-, Ni-, and Cu- (Rad et al., 2020; Xu et al., 2022). However, monometallic catalysts often encounter suboptimal cycling efficiency and ion leaching issues, constraining their practical applications (Duan et al., 2015; Wang et al., 2024a). In contrast, the synergistic effect of bimetallic active sites can prevent metal ion leaching and enhance electron transfer (Zhang et al., 2024). Layered double hydroxides (LDHs), known as hydrotalcite-type compounds, are two-dimensional anionic clays (Liu et al., 2024a; Long et al., 2022; Sadeghi Rad et al., 2022). Due to their remarkable dispersibility, customizable ion composition, and unique structure, LDHs are considered promising precursors for mixed metal oxides (Guo et al., 2022; Liu et al., 2024a; Long et al., 2022). LDHs and their derivatives are promising persulfate activators due to several advantages: (i) low cost and a simple production process; (ii) polyatomic interactions, which allow the preparation of LDHs using a variety of transition metals and functional anions to enhance the catalytic performance of the material; (iii) favorable fixation effect for metal ions due to the stabilized structure of LDHs (Jawad et al., 2015); (iv) diversity of morphology, which can be modified by calcination to increase active sites and improve catalytic properties (Boccalon et al., 2020; Hong et al., 2020). For example, Wang et al. effectively degraded norfloxacin using $SO_4^{\cdot-}$ and $^1O_2$ produced by AlCo-LDH/seafoam activating PMS (Wang et al., 2024c). Yang et al. prepared oxygen vacancy-rich Fe-Ni-LDH-activated PMS for the degradation of tetracycline hydrochloride and found that under the optimal conditions, there was a 4-fold enhancement compared to the unmodified material, and it showed stable and efficient performance in continuous flow experiments (Yang et al., 2024b).

Although 2D LDH nanosheets perform excellently in various applications, they are prone to stacking and aggregation, which restricts ion migration and limits their practical utility (Fu et al., 2022; Ma et al., 2021; Qian et al., 2023; Theerthagiri et al., 2021). In contrast, 3D materials have a larger specific surface area and multilevel pore structure, facilitating better contaminant adsorption and electron transfer (Zhu et al., 2020). The 3D morphology influences adsorption, mechanical resistance, thermal stability, and surface capacity. Ammonium fluoride (NH_4F) can act as a morphological control agent to synthesize catalysts with different structures (Yan et al., 2021). For example, Li et al. utilized ammonium fluoride to construct a 3D porous LDH/PVDF foam. The prepared 3D morphology $Co_5Fe_{2.5}$LDH(F)/PVDF had increased active sites, and the metal ion charge distribution was adjusted according to the metal-F coordination to expose more Co sites. The optimized $Co_5Fe_{2.5}$LDH(F)/PVDF foam demonstrated long-term, high degradation rates for simulated dye-contaminated river water (Li et al., 2021a). Similarly, Yang et al. developed FeCoNi LDH/NF-3.0 nM with laminated nanosheets and nanoflower coexisting structures in the presence of ammonium fluoride. This structure enhanced the number of active sites and promoted electron transfer, thereby accelerating the oxygen evolution reaction (OER) (Yang et al., 2024a). These findings show that different morphologies significantly influence material properties and the metal migration mechanism during bimetallic degradation of pollutants. Therefore, the catalyst activity can be improved by designing effective morphologies and further studying their activation and degradation mechanisms.

In this study, the spherical Fe-Mn LDH (S-FML) structure was

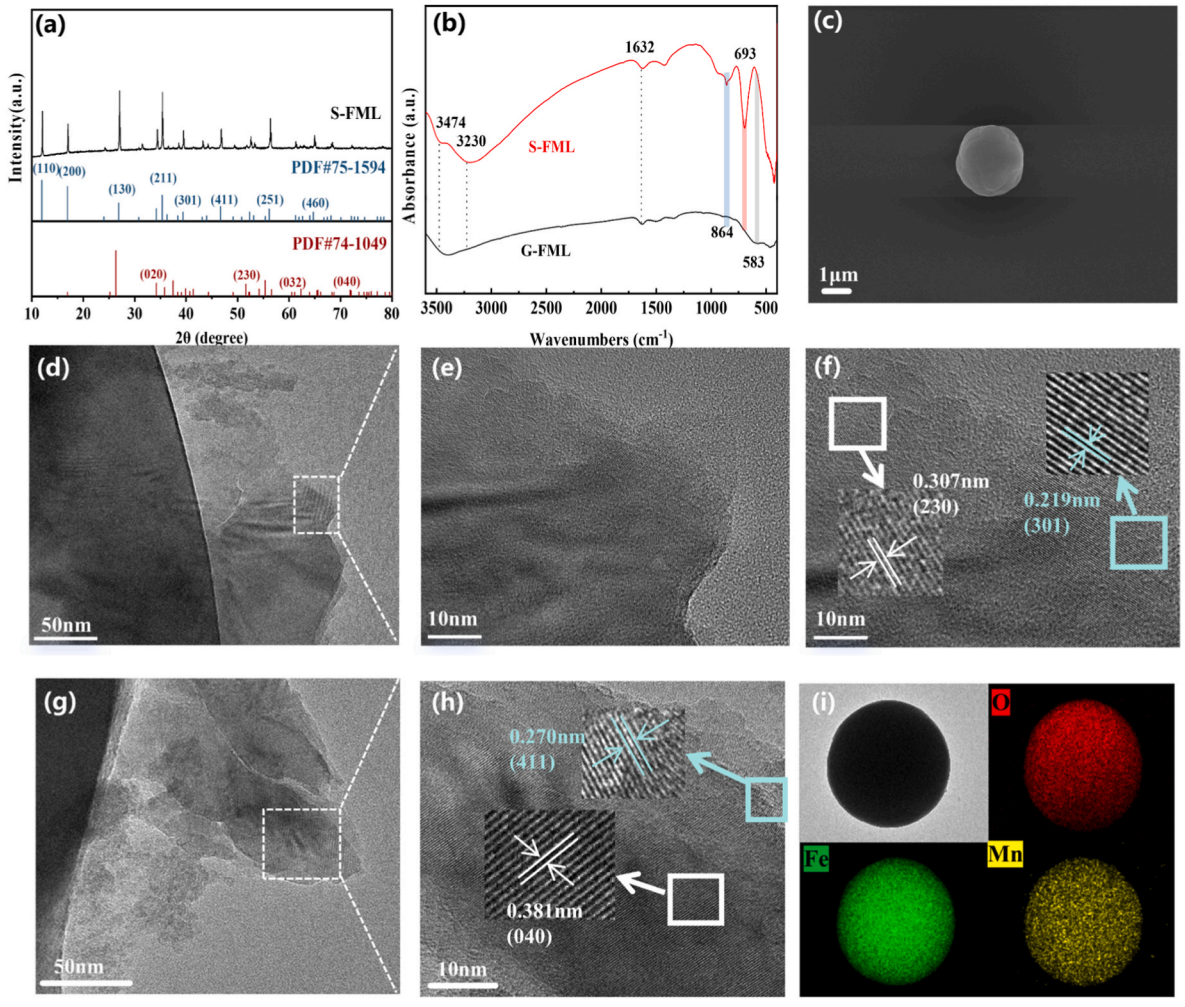

Fig. 1. (a)XRD of S-FML. (b) FT-IR of S-FML and G-FML (c) SEM of S-FML. (d–h) TEM of S-FML. (i) EDS elemental mapping of the S-FML.

synthesized by a modified hydrothermal method. Iron and manganese were chosen for their effectiveness in activating transition metals in PI (Cao et al., 2024; Zeng et al., 2024), while the spherical structure minimizes stacking. This research focused on three main objectives: (i) systematically evaluating the catalytic activity of the S-FML/PI system, including its suitability and material stability in various aqueous matrices and against different organic pollutants. (ii) elucidating the degradation mechanism of SIZ, driven by the primary active species $^1O_2$ and IO_3. (iii) determining degradation pathways and assessing degradation product toxicity using DFT and intermediate product analysis. This work aims to provide a theoretical foundation for PI-based Fenton-like reactions and degradation methods, contributing to the development of advanced pollutant removal techniques for wastewater treatment.

2. Materials and methods

2.1. Experimental materials

The chemical list is provided in Text S1.

2.2. Preparation of S-FML

S-FML was primarily developed following the approach of Xu et al. (2022). Briefly, 2.020 g of iron (III) nitrate nonahydrate, 0.178 g of manganese nitrate hydrate, 0.296 g of ammonium fluoride, and 0.720 g of urea were added to a 100 ml beaker containing 50 ml of ultrapure water and magnetically stirred for 30 min. The mixed solution was transferred into a polytetrafluoroethylene liner and heated at 120 °C for 12 h. After the reaction, the mixture was centrifuged, washed with water and ethanol, and dried at 60 °C for 12 h. The red-brown solid obtained was identified as S-FML. The preparation of granular Fe-Mn LDH (G-FML) is principally achieved through coprecipitation, with further details provided in Text S2.

2.3. Experimental procedure

The reaction was conducted in a 100 ml beaker, where 10 mg of catalyst was weighed and 50 ml of a 10 mg/L SIZ solution was added. The mixture was magnetically stirred for 10 min to achieve adsorption-desorption equilibrium, after which 0.25 mL of a 100 nM PI solution was added. Samples were collected at designated time points by adding 100 μL of a 100 mM sodium thiosulfate solution. The reaction was terminated, then filtered through a 0.22 μm needle filter and added to the sample vial, and subsequently analyzed by high-performance liquid chromatography (HPLC, LC-20, SHIMADZU, Japan). To minimize systematic errors, all degradation experiments were repeated at least three times. The intermediates generated by SIZ during degradation were identified using high-performance liquid chromatography-tandem mass spectrometry (HPLC/MS, Thermo, USA). Further instrumentation and characterization methods are detailed in Text S3.

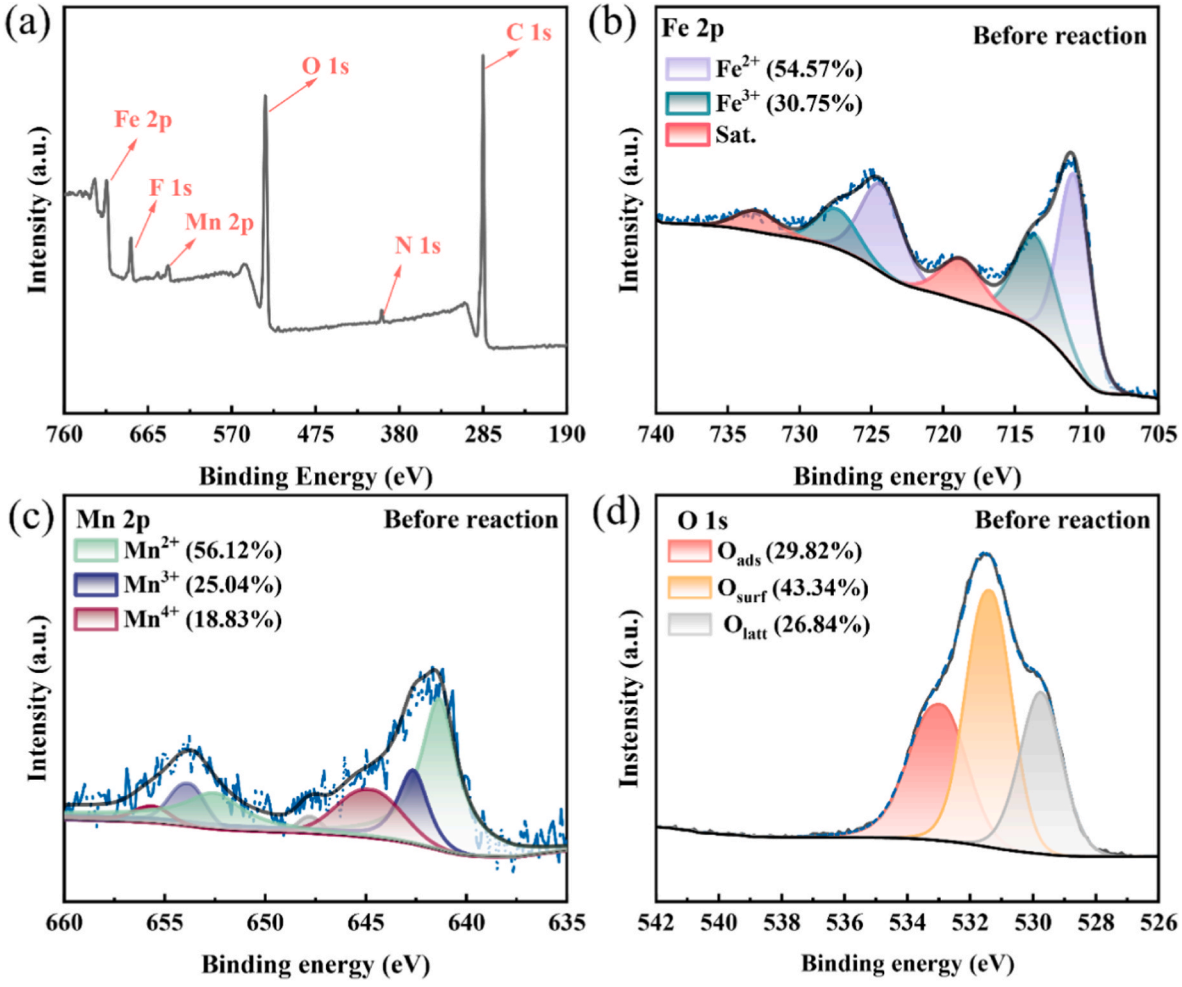

Fig. 2. High-resolution XPS spectra for (a) total spectrum, (b–d) Fe 2p, Mn 2p, and O 1S of the S-FML.

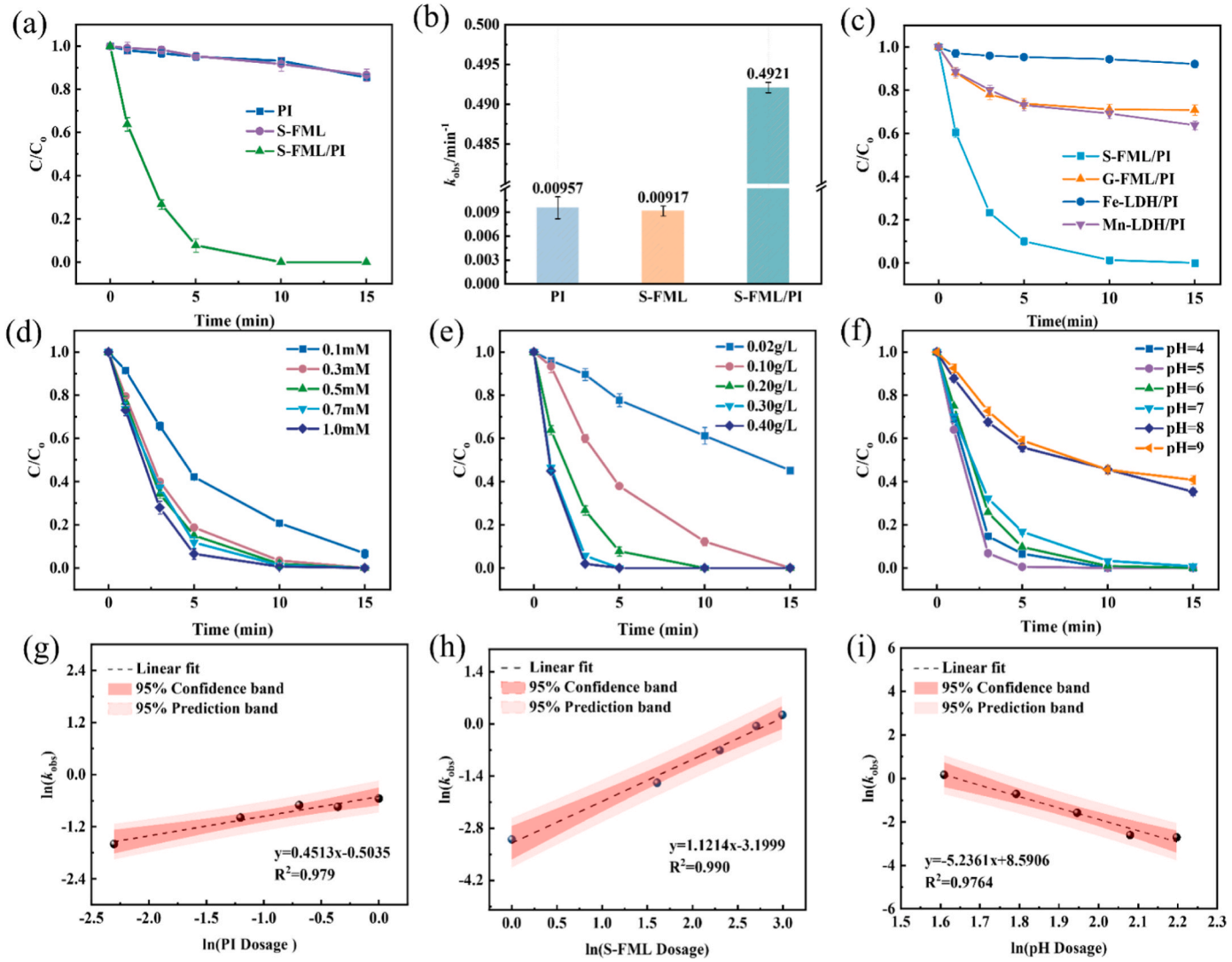

Fig. 3. (a) Ability of each experimental group to degrade SIZ. (b) The first-order kinetic constant k_{obs} of various experimental groups to degrade SIZ. (c) The ability of materials prepared with different morphologies and elements to degrade SIZ. (d–f) The degradation ability of S-FML/PI under different conditions (d) PI dosage, (e) catalyst dosage, (f) different pH environments. (g–i) Logarithmic relationship between S-FML activated PI for degradation of SIZ, (g) logarithmic relationship between ln(k_{obs}) and ln(PI dose. (h) logarithmic relationship between ln(k_{obs}) and ln(S-FML dosage). (i) logarithmic relationship between ln(k_{obs}) and ln(pH). Reaction conditions: [SIZ] = 10 mg/L, [PI] = 0.5 mM, [catalyst] = 0.20 g/L.

2.4. Methods of calculation and analysis

The present calculations were carried out using the Gaussian 09 program fully optimized at the B3LYP/6-31G* level of theory on the structure of the studied complexes for the study of the molecular orbital levels of the SIZ, which include the highest occupied molecular orbital (HOMO) and the lowest unoccupied molecular orbital (LUMO). The Hirshfeld atomic charges and Fukui indices (f^+, f^-, f^0, and CDD) of the molecules were calculated and analyzed using the Multiwfn software (Lu and Chen, 2012; Lu and Chen, 2022).

Toxicity prediction of intermediates produced during degradation of SIZ using the Ecological Structure Activity Relationships (ECOSAR) program (version 1.11) was used to understand the effects of intermediates on green algae, Daphnia, and fish in the water column. Mainly acute toxicity (LC_{50}) and chronic toxicity (Ch V) were evaluated separately (Li et al., 2021b).

3. Results and discussion

3.1. Characterization of materials

The crystal characteristics of S-FML were analyzed using X-ray diffraction (XRD) (Fig. 1a), which showed that the prepared S-FML has diffraction peaks at 11.9°, 16.9°, 26.8°, 29.2°, 35.3°, 46.6°, 56.1°, and 64.0°, which correspond to the (100), (200), (130), (211), (301), (411), (251), and (460) crystallographic planes of FeOOH (PDF#75–1594), respectively. Additionally, the peaks at 31.6°, 52.4°, 61.2°, and 72.0° align with the (020), (230), (032), and (040) crystal planes of Mn(OH)O (PDF#74–1049), respectively. These results indicate that S-FML primarily consists of FeOOH and Mn(OH)O. G-FML, prepared by the conventional co-precipitation method, displayed diffraction peaks at 2θ = 24.2°, 37.5°, 41.4°, and 51.5°, corresponding to the (012), (110), (113), and (018) planes, respectively (Fig. S1). This result was consistent with the Mn-Fe LDH synthesized by Hou et al. (2019), confirming the successful synthesis of G-FML. However, the material exhibited low crystallinity. In contrast, the diffraction peaks of S-FML were sharper, indicating a higher degree of crystallinity and potentially enhanced

degradation properties (Deng et al., 2017).

Fourier transform infrared (FT-IR) spectroscopy was used to analyze the functional groups of S-FML samples prepared by different synthetic methods (Fig. 1b). It was established that both samples exhibited characteristic surface hydroxyl peaks (-OH) at 1632 cm^{-1}, 3474 cm^{-1}, and 3230 cm^{-1} (Chen et al., 2024d; Wang et al., 2020). Different preparation methods may result in different yields of M-OH (M = Fe or Mn), whereas the higher ambient temperature of the preparation of S-FML may result in predominantly Fe-OH binding to the material within the system. (Mochizuki et al., 2021). Thus, in contrast to S-FML, G-FML exhibited a distinctive Fe-O peak at 586 cm^{-1} (Guo et al., 2021), while the Fe-OH peak at 693 cm^{-1} was absent (He et al., 2021). Additionally, the intensity of the Mn-OH stretching peak at 864 cm^{-1} was lower in G-FML than in S-FML, suggesting that S-FML contains a greater abundance of Mn-OH bonds (Hou et al., 2019). Overall, S-FML exhibited a higher concentration of surface hydroxyl groups, with more Fe-OH and Mn-OH than G-FML, potentially enhancing the decomposition of PI (Pan and Xing, 2008).

Scanning electron microscope (SEM) was used to examine the morphology and structure of S-FML (Fig. 1c). The material was observed to have a spherical shape with a radius of approximately 1 μm. In contrast, G-FML prepared via co-precipitation exhibited considerable collapse and agglomeration, which could reduce the exposure of active sites and consequently decrease its degradation capacity (Fig. S2) (Xiong et al., 2022). This suggests that S-FML, synthesized via the hydrothermal method, exhibits superior dispersion and may interact more effectively with PI for activation.

The microstructure of S-FML was further examined using transmission electron microscopy (TEM) (Fig. 1d–h). and the lattice stripe spacings calculated from the edges were 0.219 nm and 0.270 nm for (301) and (411) planes of FeOOH, respectively. Similarly, 0.307 nm and 0.381 nm corresponded to the (230) and (040) planes of Mn(OH)O. These results confirmed the compositional structure of S-FML. The elemental composition of the material was analyzed using energy-dispersive X-ray spectroscopy (EDS) (Fig. 1i and Fig. S3), revealing a uniform distribution of Fe, Mn, and O elements.

X-ray photoelectron spectroscopy (XPS) was used to investigate the chemical states of the elements in S-FML. As shown in Fig. 2a and Fig. S4, the XPS spectrum of S-FML displayed distinct peaks for O 1s, Mn 2p, and Fe 2p (Han et al., 2022), confirming the successful incorporation of Fe and Mn. The binding energies of the specific elemental peaks are provided in Table S2. Fig. 2b shows the high-resolution Fe 2p spectrum, wherein the peaks of Fe^{2+} were observed at 710.86 eV and 724.30 eV, the peaks of Fe^{3+} were seen at 713.55 eV and 727.37 eV, and the satellite peaks were observed at 718.76 eV and 733.01 eV (Cheng et al., 2024; Long et al., 2024). Fig. 2c shows the high-resolution Mn 2p spectrum, where 641.83 eV and 652.40 eV are associated with the Mn^{2+} peak, 642.78 eV and 654.09 eV correspond to the Mn^{3+} peaks, and 645.70 eV and 655.98 eV are related to the Mn^{4+} peak (He et al., 2024). Fig. 2d shows the O 1S spectra, where peaks at 529.64 eV, 531.46 eV, and 533.74 eV were associated with lattice oxygen (O_{latt}), surface hydroxyl (O_{surf}), and adsorbed oxygen (O_{ads}), respectively, as previously defined in the literature (Han and Xiao, 2022; He et al., 2020). The XPS results confirmed the successful synthesis of S-FML and the presence of Fe and Mn in multiple valence states Furthermore, the diverse valence states of Fe and Mn in the bimetallic material enable redox cycling, which promotes PMS activation (He et al., 2024).

3.2. Performance of S-FML in Fenton-like reactions

A series of kinetic experiments were performed to assess the degradation efficiency of the S-FML/PI system. As shown in Fig. 3a, the combination of S-FML and PI resulted in the complete degradation of SIZ within 15 min. The data were analyzed using pseudo-first-order kinetics, yielding a rate constant of 4.96×10^{-1} $min^{-1}$for SIZ degradation in the S-FML/PI system, approximately 51 times higher than that for S-FML and PI alone (Fig. 3b). This can be attributed to the low oxidation potential of IO_4^-, which has minimal impact on SIZ degradation (He et al., 2022). S-FML also showed a slight adsorption effect, adsorbing SIZ onto its surface and enhancing its degradation capacity after activation by PI. This demonstrated that the S-FML/PI system played a key role in promoting SIZ degradation by generating more active species, resulting in rapid degradation within a short timeframe.

Both Fe and Mn are excellent PI activators, with Mn being the most potent (Du et al., 2019; Xu et al., 2023). To assess the individual effects of Fe and Mn, Fe-LDH and Mn-LDH were synthesized separately and tested under identical experimental conditions (Fig. 3c). The results showed that the bimetallic S-FML exhibited superior degradation performance compared to the single-metal Fe-FML and Mn-FML. The combination of Fe and Mn in the S-FML/PI system also produced a synergistic effect. Notably, the S-FML/PI system demonstrated a first-order kinetic constant approximately 17 times higher than that of G-FML, indicating significantly better degradation performance. In conclusion, S-FML outperforms other systems, and the synergistic effect between Fe and Mn plays a crucial role in its enhanced degradation performance.

3.3. Influencing parameters of the reaction process

3.3.1. The impact of catalyst and oxidizer dose

Fig. 3d shows the results of the degradation experiments with varying PI doses, indicating a positive correlation between PI concentration and SIZ removal at oxidant concentrations from 0.1 to 0.5 mM. This correlation was due to the increased PI concentration, which led to the production of more active species. To assess the sensitivity of SIZ degradation, a linear fit was applied to $\ln(k_{obs})$ against the logarithm of PI dosing (ln (PI dosing)). The slope for the PI dosage was found to be low (0.4513, Fig. 3g). The enhancement of the kinetic rate constants became negligible at PI dosages above 0.5 mM, as shown in Fig. S5. This phenomenon is likely due to radical-radical recombination, which can occur when the radical concentration in AOPs becomes too high (Eqs. (1)–(3)) (Huang et al., 2024).

The effect of S-FML concentration on the degradation rate was evaluated (Fig. 3e), showing that the SIZ degradation rate increased with higher catalyst concentrations. was completely degraded within 15 min at all catalyst dosages, except for 0.02 g L^{-1}. This was due to higher catalyst concentrations providing more active sites, thus enhancing PI activation efficiency. In addition, the slope of correlation (1.1214, Fig. 3h) was obtained by linear fitting of $\ln(k_{obs})$ and the logarithm of the material dosage (ln (S-FML dosage)). From the perspective of degradation rate constants, it was found that the kinetic rate constants increased rapidly with the increase in catalyst dosage. However, as the catalyst concentration continued to increase, the rate of increase in degradation slowed. This was likely due to S-FML aggregation at higher concentrations, which reduced the exposure of surface reactive sites. Based on these findings, subsequent experiments used a reduced catalyst dosage of 0.2 g L^{-1} and an optimal PI concentration of 0.5 mM.

3.3.2. The impact of pH

The pH of the water is a critical factor influencing the AOP process (Yeon et al., 2022). Fig. 3f shows the degradation of SIZ by the S-FML/PI system under varying pH conditions (4, 5, 6, 7, 8, and 9). The SIZ degradation rate constant at pH = 5 was 1.9 times higher than that at pH = 4 (Fig. S6), contrary to the expectation that lower pH would improve degradation. This result is likely due to excess H^+ ions, which generate H· that reacts with IO_3^- reducing active species yield (Eq. (4)) and lowering performance (Zeng et al., 2024). The system also showed reduced SIZ degradation in alkaline conditions, likely due to elevated pH causing IO_4^- to convert to $H_2I_2O_{10}^{4-}$, which has lower reactivity and redox potential (Eqs. (5)–(7)) (Bokare and Choi, 2015; He et al., 2021). Overall, the S-FML/PI system was more effective under acidic conditions, achieving significant SIZ degradation within 15 min. The sensitivity of

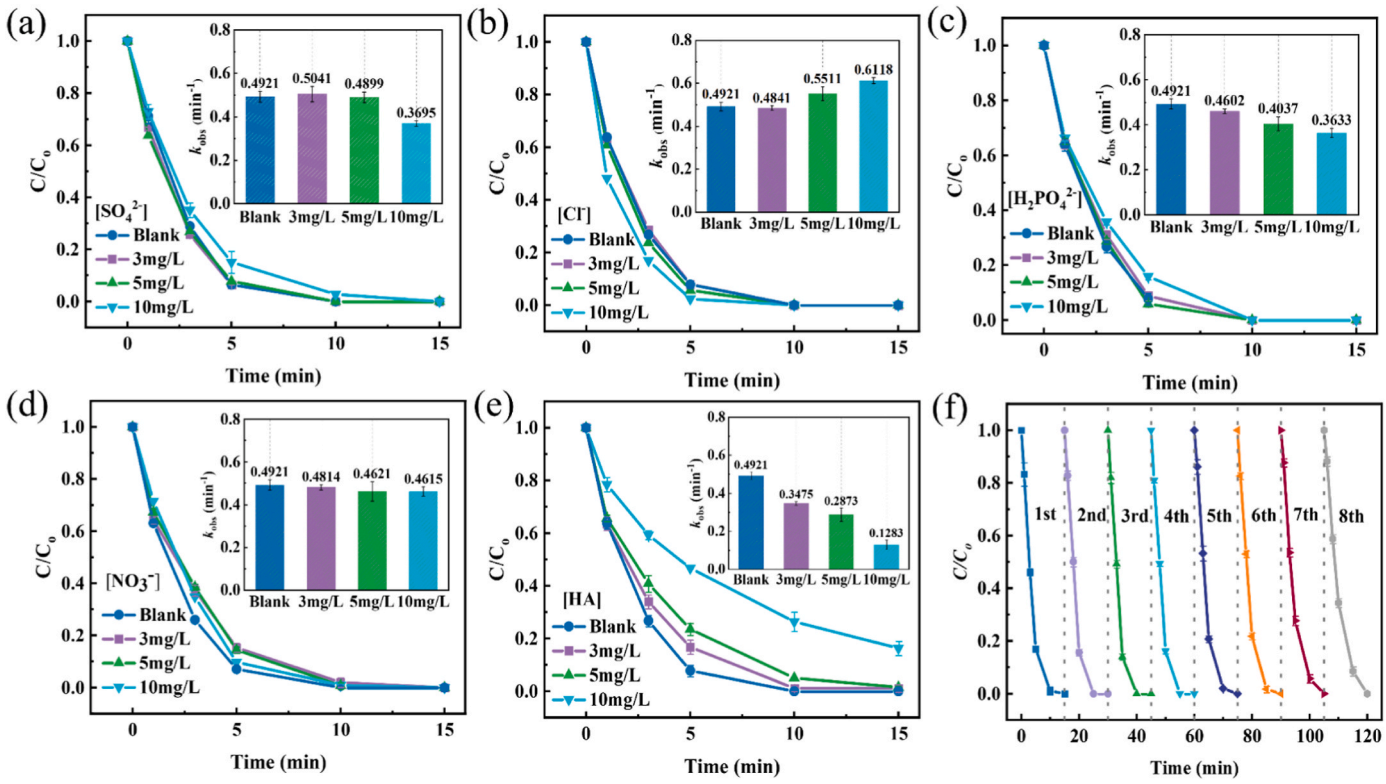

Fig. 4. (a–e) Under the influence of SO_4^{2-}, Cl^-, $H_2PO_4^-$, NO_3^- and HA at different concentrations, respectively. (f) Continuous operation of the S-FML/PI system. Reaction conditions: [SIZ] = 10 mg/L, [PI] = 0.5 mM, [catalyst] = 0.20 g/L.

SIZ degradation to pH changes was quantified by a slope of 5.2361 (Fig. 3i), indicating that pH significantly influences SIZ degradation in the S-FML/PI system. Subsequent exploration of pH changes during the reaction of the S-FML/PI system revealed that the pH hardly changed throughout the experiment. (Fig. S7).

The impact of pH on the S-FML/PI system was further investigated using zeta potential analysis (Fig. S8). The point of zero charge (pH_{pzc}) for S-FML was 7.26. This suggests that the S-FML surface is positively charged when the pH is below 7.26 and negatively charged when the pH exceeds 7.26. According to the literature, the dissociation constants of SIZ are pKa1 = 4.79 and pK2 = 5.0. In this system, at pH < 7.26, the positively charged surface of S-FML promotes electrostatic attraction with the SIZ anion, facilitating interaction. After pH 7.26, the negatively charged surface of S-FML inhibits interaction with SIZ anions, contributing to further pH increases.

The above conclusions summarize the three main factors influencing SIZ degradation sensitivity (Fig. S9). The contribution of pH to the degradation process was 76.9%, significantly higher than that of S-FML dosage (16.5%) and PI dose (6.6%). This indicates that pH is the most significant factor influencing the S-FML/PI system's ability to remove SIZ.

$$IO_4^- + IO_3\cdot \rightarrow IO_4\cdot + IO_3^- \quad (1)$$

$$2IO_3\cdot \leftrightharpoons I_2O_6 \quad (2)$$

$$2IO_4\cdot \leftrightharpoons I_2O_8 \quad (3)$$

$$H\cdot + IO_3\cdot \rightarrow IO_3^- + H^+ \quad (4)$$

$$H_4IO_6^- \leftrightharpoons H_3IO_6^{2-} + H^+ \quad (5)$$

$$H_4IO_6^- \leftrightharpoons IO_4^- + 2H_2O \quad (6)$$

$$2H_3IO_6^{2-} \leftrightharpoons H_2I_2O_{10}^{4-} + 2H_2O \quad (7)$$

3.4. Universality of S-FML/PI

3.4.1. Effect of anions

To evaluate the impact of common anions and natural organic matter on the effectiveness of the S-FML/PI system, the influence of several anions (Cl^-, $H_2PO_4^-$, SO_4^{2-}, NO_3^-) and humic acid (HA) on SIZ degradation in water was examined (Mi et al., 2022; Theerthagiri et al., 2022b). It was found that SO_4^{2-}, being an inert ion, did not affect the degradation of SIZ (Fig. 4a) (Gong et al., 2024). As a result, varying concentrations of SO_4^{2-} had negligible impact on SIZ degradation. Furthermore, the presence of Cl^-, $H_2PO_4^-$, and NO_3^- has a minimal impact on the degradation of SIZ in the system. This can be attributed to free radicals generated in the system reacting with Cl-to form chlorine-containing reactive species (Eq. (8)) (Fig. 4b) (Li et al., 2024), thereby aiding SIZ degradation. The $H_2PO_4^-$ generated from the ionization of $H_2PO_4^-$ reacted with ·OH to form HPO_4^- (Eqs. (9) and (10)) (Fig. 4c), and the reaction of IO_4^- and NO_3^- products to produce low activity $NO_3\cdot$ (Eq. (11)) (Fig. 4d) (Wang et al., 2024b). Overall, the S-FML/PI system exhibited good resistance to common anions The impact of HA, a commonly found dissolved organic matter (DOM) in natural water bodies, on SIZ degradation in the S-FML/PI system was also investigated (Fig. 4e). The results indicated that the presence of HA had some inhibitory effect on the system, with SIZ degradation still at about 84% under the influence of 10 mg/L HA. This suggests that DOMs exert a stronger inhibitory effect on the system. This could be due to HA adsorbing onto S-FML, reducing available active sites and contact with PI, thereby lowering active species production (Xu et al., 2023). Alternatively, competition between HA and SIZ for active species may reduce the available active species to degrade SIZ (Jiang et al., 2024). In conclusion, the S-FML/PI system remains effective in degrading SIZ, even in the presence of various ionic interferences.

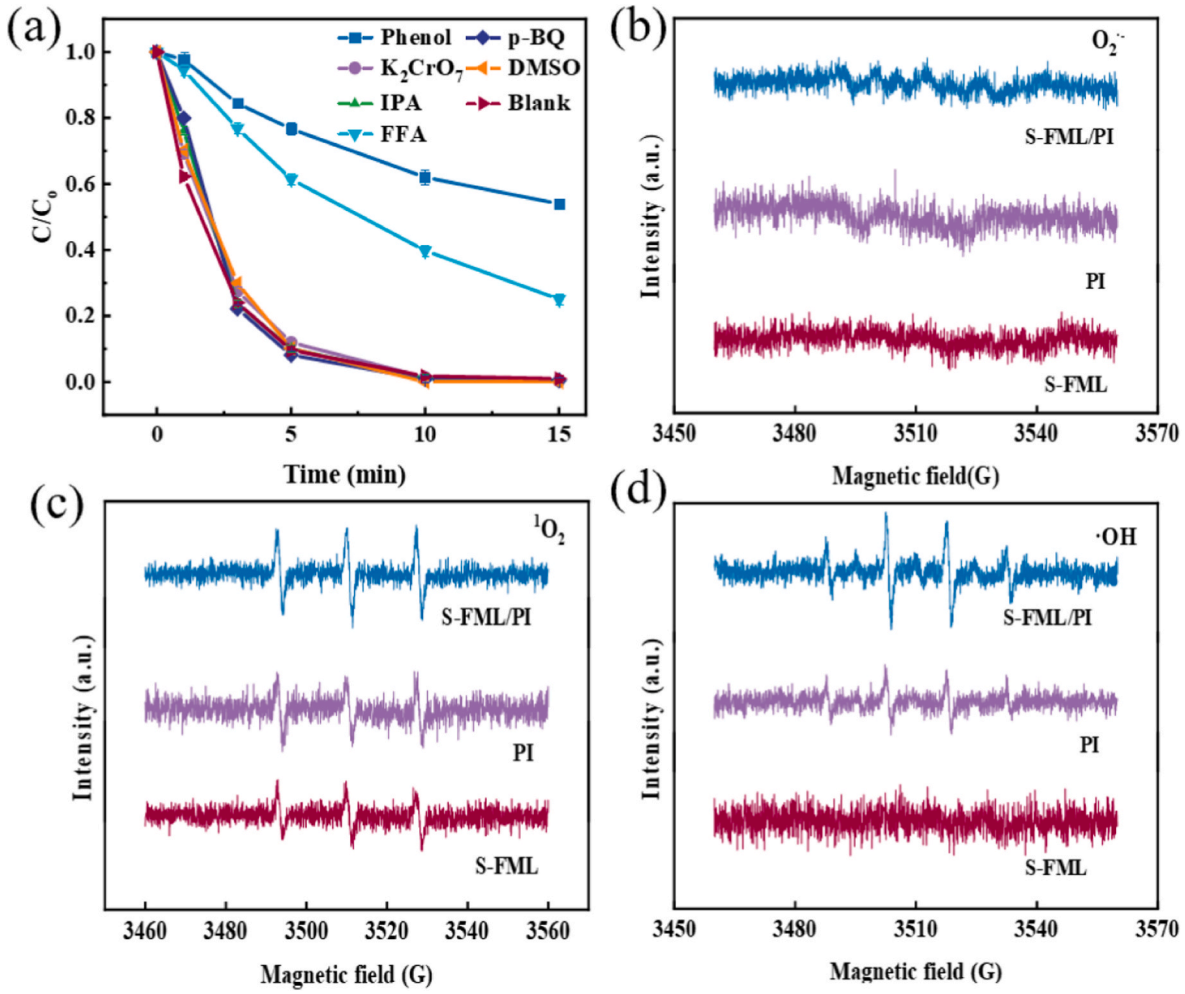

Fig. 5. (a) Effect of the presence of different quencher agents on the degradation of SIZ by the S-FML/PI system. (b) EPR spectra of S-FML/PI system DMPO-O_2^-, (c) TEMP-$^1O_2$, (d) DMPO-·OH.

$$Cl^- + \cdot OH \rightarrow HOCl\cdot^- \quad (8)$$

$$H_2PO_4^- \rightarrow H^+ + HPO_4^{2-} \quad (9)$$

$$HPO_4^{2-} + \cdot OH \rightarrow HPO_4^-\cdot + OH^- \quad (10)$$

$$IO_4^- + NO_3^- + H_2O \rightarrow IO_3\cdot + NO_3\cdot + 2OH^- \quad (11)$$

3.4.2. Degradability and stability

Material stability is a crucial factor in evaluating its practical applicability. The post-reaction solution was filtered, and the metal content was analyzed using ICP-OES/MS, revealing 0.0118 mg/L of manganese and 0.0174 mg/L of iron. (Table S3). To assess the stability and reusability of S-FML, eight consecutive cycles were performed (Fig. 4f). The results showed that while S-FML maintained stable performance over eight cycles, a slight reduction in degradation efficiency was observed. In each cycle, SIZ was completely degraded within 15 min, demonstrating the excellent stability of S-FML.

The performance of the S-FML/PI system was evaluated through comparative degradation tests involving different sulfonamide pollutants: sulfadiazine (SDZ), sulfamethazine (SMR), and sulfamethoxazole (SMT). The degradation results, as shown in Fig. S10, demonstrate that the S-FML/PI system effectively degraded SDZ and SMR, achieving over 99% removal within 15 min. Moreover, SMT was degraded by 71% during the same time period.

The practical application potential of the S-FML/PI system was then evaluated using real water samples. As shown in Fig. S11, the S-FML/PI system demonstrated excellent degradation performance in all three water bodies. However, the degradation rates varied among the three water bodies, likely due to the presence of various ions and organic matter, which may hinder the degradation of SIZ by IO_3·. In conclusion, the system has demonstrated strong resistance to interference and holds promise as an effective catalytic solution for addressing pollution in natural environments.

3.5. Mechanism exploration

3.5.1. Free radical detection

To understand the degradation pathway of the S-FML/PI system, it is essential to identify the reactive species generated during the system's reactions. Each reactive species (ROS (·OH, $O_2\cdot^-$, $^1O_2$), RIS (IO_3·, IO_4·) and (electron transfer)) generated in the system may significantly contribute to pollutant degradation (Du et al., 2020). Therefore, different quenchers are utilized to determine the reactive species generated by the system as a practical approach to exploring the degradation pathway of the S-FML/PI system. Quenching experiments were conducted to assess the quenching effects of furfuryl alcohol (FFA), phenol (Chen et al., 2024a), isopropyl alcohol (IPA) (Gao et al., 2022), p-benzoquinone (p-BQ) (Fang et al., 2022), K_2CrO_7 (He et al., 2022), and dimethyl sulfoxide (DMSO) (Zong et al., 2021) on $^1O_2$, IO_3^-, ·OH, $O_2\cdot^-$, e^-, and Fe(IV), respectively. As shown in Fig. 5a and Fig. S12, the degradation of the S-FML/PI system reduced from 100% to 73.45% and

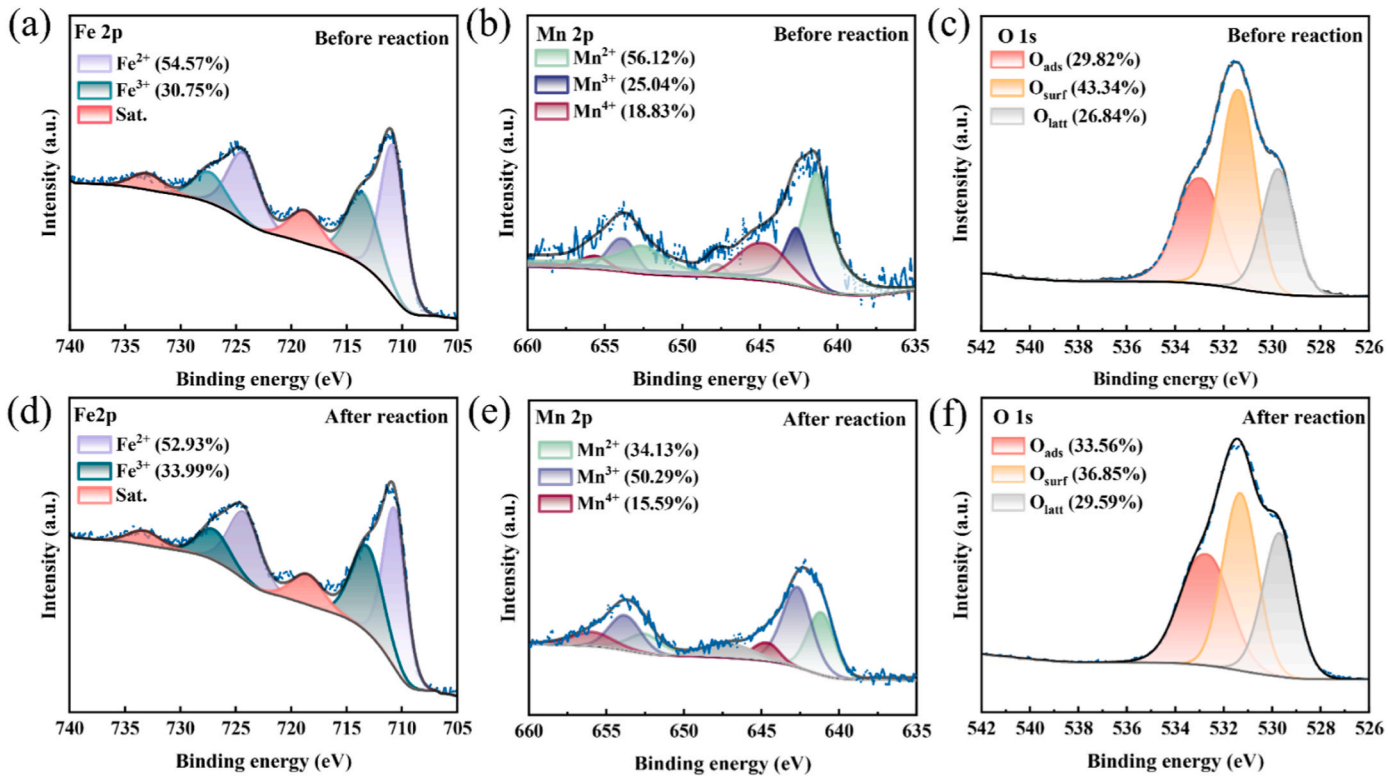

Fig. 6. (a–c) XPS patterns of Fe 2p, Mn 2p, and O 1s in S-FML before reaction. (d–f) XPS patterns of Fe 2p, Mn 2p, and O 1s in the reacted S-FML.

46.75% with the addition of FFA and phenol, respectively. The effects of the other quenchers were minimal, indicating that ·OH, $O_2{\cdot}^-$, e^-, and Fe (IV) made only a minor contribution to the degradation of the S-FML/PI system (Chen et al., 2024c; Shen et al., 2023).

The presence of free radicals ($O_2{\cdot}^-$,$^1O_2$, and ·OH) was further demonstrated by electron spin resonance (EPR) experiments using DMPO and TEMP as trapping agents to directly detect the reactive species generated in the system. The characteristic signal peaks of $O_2{\cdot}^-$, $^1O_2$, and ·OH were observed respectively (Fig. 5b–d), and it was further proved that $O_2{\cdot}^-$ is not the active species acting in the system, as shown in Fig. 4b. According to Fig. 4c–d, the EPR signal peaks in the S-FML/PI system were characterized by distinct patterns: 1:1:1 for TEMP-$^1O_2$and 1:2:2:1 for DMPO-·OH signals (Lin et al., 2023). The presence of $^1O_2$ and ·OH in the system was confirmed. The relatively low concentration of ·OH was found to account for the decrease in the reaction rate constant (4.59×10^{-1} min^{-1}) observed after adding IPA, compared to the control group. Therefore, it can be concluded that $^1O_2$ and $IO_3{\cdot}$ played a critical role in the degradation of SIZ.

3.5.2. *Activation mechanism*

To further elucidate the catalytic mechanism, X-ray photoelectron spectroscopy (XPS) was employed to examine the chemical composition and elemental valence states of both the fresh and reacted Fe-Mn-LDH. Changes in the Fe 2p spectrum of S-FML were examined (Fig. 6a and d). The analysis showed that the binding energy values of the elements remained largely unchanged before and after the reaction. Percentage changes in the Fe 2p spectra of Fe^{2+} and Fe^{3+} before and after the reaction were related to their contributions to PI. Among the observed changes, the percentage of Fe^{2+} decreased from 54.57% before the reaction to 52.93%, while the percentage of Fe^{3+} increased from 30.75% to 33.99%. This suggests that Fe plays a role in the degradation process of SIZ and may serve as an active site for PI activation (Ling et al., 2022). Fig. 6b and e show high-resolution Mn 2p spectra before and after the reaction. The contents of Mn^{2+}, Mn^{3+}, and Mn^{4+} changed before and after the reaction. Specifically, Mn^{2+} decreased from 56.12% to 34.13%, Mn^{3+} increased from 25.04% to 50.29%, and Mn^{4+} decreased from 18.83% to 15.59%. Fig. 6c and f show the O 1s spectra before and after the reaction. After the reaction, the O_{latt} peak increased from 26.84% to 29.59%. O_{surf} decreased significantly from 43.34% to 36.85% and O_{ads} increased from 29.82% to 33.56%. This may be because -OH in O_{surf} is an electron-rich group that acts as an active site (Zheng et al., 2022). The decrease in O_{surf} may result from its involvement in the degradation process (Liu et al., 2020). The increase in O_{ads} may be attributed to the formation of additional metal-oxygen bonds on the catalyst surface during the reaction (Chen et al., 2024b).

The reaction mechanism of the S-FML/PI system can be summarized as follows based on the above conclusions: (1) $IO_3{\cdot}$ was converted by PI, and $IO_3{\cdot}$ could react with IO_4^- to form $IO_4{\cdot}$, which reacted with itself to form $^1O_2$ (He et al., 2022; Gong et al., 2023) (Eqs. (12)–(14)). (2) Mn^{3+} and Mn^{4+} may also be involved in the conversion reactions (Zhang et al., 2021). Specifically, Mn^{3+} could react with IO_4^- to form $IO_3{\cdot}$ (Yu et al., 2023) (Eqs. (14)–(17)). (3) Fe^{2+} could activate PI to produce $IO_3{\cdot}$ and ·OH (Li et al., 2024) (Eqs. (18) and (19)). Finally, in both homogeneous and heterogeneous reactions, the standard reduction potential of Fe^{2+}/Fe^{3+} (0.77 eV) (0.77 eV) is higher than that of Mn^{4+}/Mn^{3+} (0.15 eV), suggesting a synergistic interaction between Fe and Mn in the system (Jin et al., 2022). The poorer activation effects of Fe-LDH and Mn-LDH compared to S-FML may also reflect the synergistic effect between Fe and Mn. The reaction between Mn^{3+} and Fe^{2+} results in the formation of Mn^{2+} and Fe^{3+} (Eq. (20)).

$$IO_4^- + 2H^+ \rightarrow IO_3{\cdot} + H_2O \quad (12)$$

$$IO_3{\cdot} + IO_4^- \rightarrow IO_4{\cdot} + IO_3^- \quad (13)$$

$$2IO_4{\cdot} \rightarrow 2IO_3^- + {}^1O_2 \quad (14)$$

$$Mn^{3+} + e^- \rightarrow Mn^{2+} \quad (15)$$

$$2Mn^{3+} + 2H_2O \rightarrow Mn^{4+} + Mn^{2+} + 4H^+ \quad (16)$$

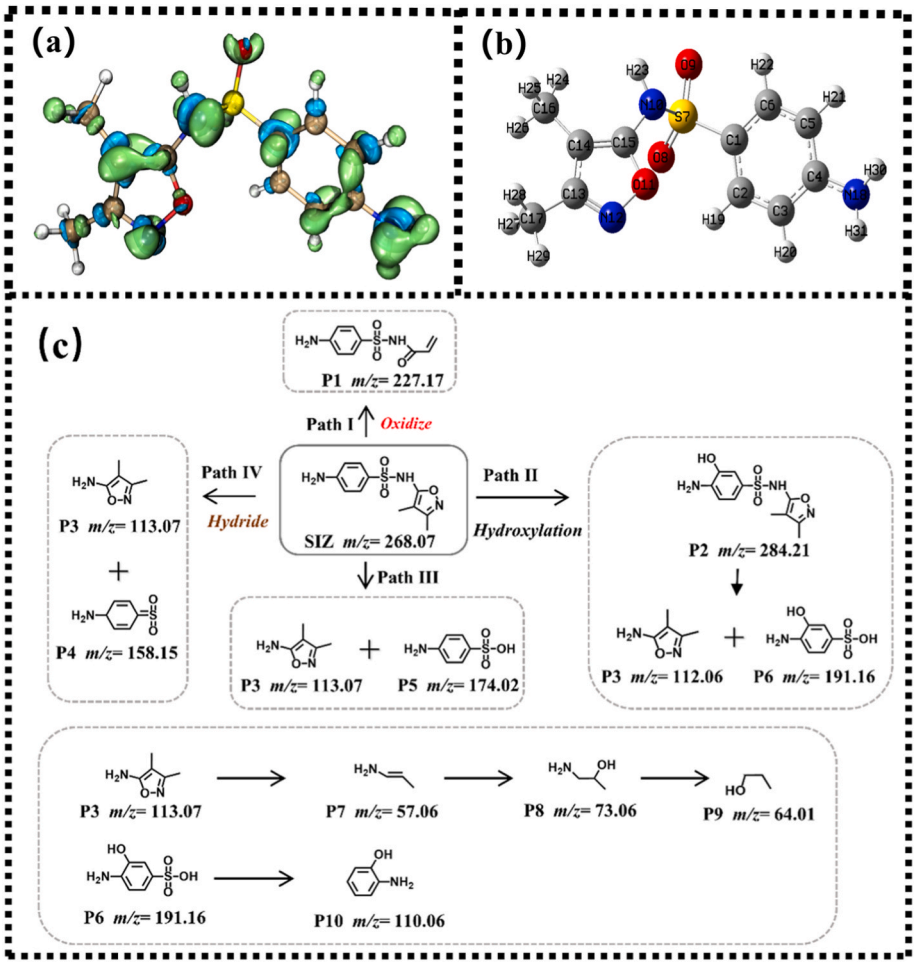

Fig. 7. (a) f-index isosurface on SIZ molecule. (b) Chemical structure and atom order of SIZ. (c) Extrapolation of possible transformation pathways of SIZ in S-FML/PI system.

$$Mn^{3+} + IO_4^- + H^+ \rightarrow Mn^{4+} + IO_3\cdot + OH^- \quad (17)$$

$$Fe^{2+} + IO_4^- + 2H^+ \rightarrow Fe^{3+} + IO_3\cdot + H_2O \quad (18)$$

$$Fe^{2+} + IO_4^- + H^+ \rightarrow Fe^{3+} + \cdot OH + IO_3^- \quad (19)$$

$$Mn^{3+} + Fe^{2+} \rightarrow Mn^{2+} + Fe^{3+} \quad (20)$$

3.6. Analysis of degradation paths

Density functional theory (DFT) was employed to further elucidate the degradation pathways and by-products, as well as to identify the reaction sites of reactive oxygen species (ROS) and free radicals on SIZ during degradation. According to the forward orbital theory (Fukui, 1970), Highest Occupied Molecular Orbital (HOMO) in the system was related to electrophilic reactions, while Lowest Unoccupied Molecular Orbital (LUMO) in the system was associated with nucleophilic reactions. In comparison, $^1O_2$ and ·OH are highly electrophilic and were more likely to attack the sites of electron density in SIZ (He et al., 2023). As shown in Fig. 7a, the HOMO of SIZ is mainly concentrated on the S-N bond and the aniline group. The electrostatic potential (ESP) of the S-N bonds, aniline, and isoxazole, located in the electron-rich regions (red regions), exhibits stronger electrophilic properties (Fig. S13) (Grimme et al., 2010; Grimme et al., 2011; Hariharan and Pople, 1973). The Fukui function was further calculated to identify the active sites of the organic molecule, where f^-, f^0, and f^+ were electrophilic, radical, and nucleophilic reactions, respectively. As seen from Fig. 7b and Table S4, f^- was higher for 5(C), 10(N), 12(N), 14(C), 18(N), and 9(O) with 0.0486, 0.0527, 0.0682, 0.0562, 0.0967, and 0.0493, respectively, which proved that electrophilic reactions were efficiently carried out at these atomic positions, and 4(C), 6(C), 7(S), 9(O), and 12(N) atomic positions had higher f^+ and were more susceptible to nucleophilic reactions, At the same time, 4(C), 9(O), 12(N), and 18(N) sites were more susceptible to radical attack. The ESP distribution of the SIZ molecules also shows that the S-N bonds, aniline, and isoxazole in the electron-rich region (red region) have better electrophilic properties.

Condensed dual descriptor (CDD) is widely accepted and reliable for predicting the reaction site position and the Fukui function method (Morell et al., 2005). The CDD was used to analyze the reaction process better (Table S4). Based on the property that the more negative CDD values were susceptible to electrophilic attack and the more positive were susceptible to nucleophilic attack, it was found that the negative CDD values were higher for 10(N), 14(C), and 18(N). In comparison, the positive CDD values were higher for 4(C), 6(C), and 7(S). The two analyses have shown a very high degree of homogeneity. Based on these results, it was concluded that the electrophilic attack mainly occurred on the benzene ring (e.g., 5(C)), amino group (e.g., 18(N)), and S-N bond (10(N)). In contrast, the benzene ring (4(C)), sulphonyl group (9(O)), and isoxazole (12(N)) were more susceptible to radical attack.

The intermediates produced during the degradation of SIZ by the S-FML/PI system were analyzed using HPLC/MS to further clarify the potential degradation pathways. As shown in Fig. 7c and Table S5, the S-N and N-O bonds in SIZ were easily broken, consistent with findings in other studies (Yao et al., 2017). Based on the analysis of these results,

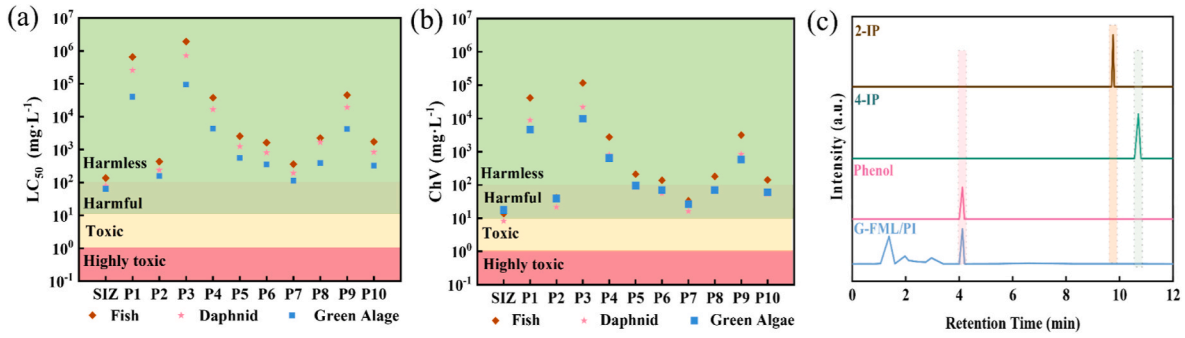

Fig. 8. (a–b) Toxicity statistics of SIZ with its intermediates as predicted by ECOSAR software. (c) detection of 2-IP and 4-IP in the system.

four potential degradation pathways for SIZ under the S-FML/PI system were proposed. In Pathway I, the O-N bond in SIZ was cleaved through oxidation to produce product P1. Pathway II involved the generation of product P2 from SIZ via hydroxylation, followed by additional hydroxylation and hydrogenation after the S-N bond was broken, forming products P3 and P6, respectively. Pathway III also involved the cleavage of the S-N bond in SIZ, resulting in the generation of products P3 and P5 through hydroxylation and hydrogenation, respectively. Pathway IV included the cleavage of the S-N bond in SIZ, followed by hydrogenation to yield products P3 and P4. Product P3 was primarily generated via continuous oxidation, forming products P7, P8, and P9. While product P6 was further oxidized, cleavage of the C-S bond was promoted to create product P10 (He et al., 2023).

3.7. Toxicity analysis

The toxicity of the intermediates generated during the reaction was predicted using ECOSAR software (Table S6), and the data were analyzed according to the Globally Harmonized System of Classification and Labeling of Chemicals (GHS), as shown in Fig. 8a and b. Fig. 8a presents the results of the acute toxicity prediction, showing that most of the intermediate products formed during SIZ degradation were non-toxic and exhibited favorable environmental properties. Fig. 8b shows the predicted chronic toxicity. Although some intermediates exhibited chronic toxicity, further reactions could reduce the toxicity of these products.

Although PI is a non-toxic oxidant, its activation can produce hypoiodous acid (HOI), I_2, and I_3^-, which may react with trace organic matter in natural waters, leading to the formation of unwanted by-products (Niu et al., 2023; Shin et al., 2018). Therefore, we investigated the types of iodine that the S-FML/PI system might generate. First, the SIZ solution degraded by the S-FML/PI system at different time points was mixed with a starch solution to check for any discoloration reaction. No discoloration was observed at any time point; the starch solution only turned blue when the iodine solution was added, confirming that I_2 and I_3^- were not produced during the reaction (Fig. S14). Additionally, as shown in Figs. 8c and 2-IP and 4-IP were not detected in the reaction system. In conclusion, the system did not generate toxic substances such as HOI and I_2.

Toxicological experiments using green beans were performed to assess the toxicity of the post-reaction solution further (Di et al., 2024) (Fig. S15). After five days of growth, the green bean lengths varied depending on the water source. Beans grown in ultrapure water had the longest length, averaging approximately 7 cm. Green beans grown in the post-reaction solution had an average length of about 6 cm, making them the second longest. Green beans grown in SIZ showed the poorest growth, with none exceeding 5 cm. This may be due to the toxicity of SIZ, which inhibits the growth of the green beans. Additionally, some intermediate products in the post-reaction solution retained a degree of toxicity, which further inhibited the growth of the green beans. Overall, the toxicity of the reacted solution was reduced.

4. Conclusions

This study developed a simple method to synthesize spherical S-FML by modulating its morphology with NH_4F, which was then used to activate PI for the degradation of SIZ. Compared to G-FML, S-FML showed improved crystallinity and enhanced Fe-OH and Mn-OH properties. S-FML also exhibited excellent stability, maintaining a 100% degradation rate of SIZ over eight cycles. The S-FML/PI system demonstrated remarkable versatility. While HA slightly inhibited the degradation process, other common anions in water had minimal impact on the system. Furthermore, the system exhibited high degradation efficiency for pollutants in real water samples, emphasizing its robust anti-pollution performance and potential for practical applications. EPR and quenching radical experiments identified $^1O_2$ and $IO_3\cdot$ as the primary reactive oxygen species (ROS) involved in the degradation of SIZ. The results indicated that the system was mainly activated by the interaction between Fe and Mn with PI on the surface of S-FML, with the valence cycling of Fe and Mn playing a key role. HPLC/MS and Fukui function analysis further elucidated the degradation pathway of SIZ. It was found that the toxicity of the intermediate products generated during SIZ degradation was lower than that of SIZ itself, and no HOI was produced. These findings confirm the efficacy and potential of the S-FML/PI system as an effective method for treating SAs.

CRediT authorship contribution statement

Junle Jian: Writing – review & editing, Writing – original draft, Validation, Investigation, Formal analysis, Conceptualization. **Siling Zhang:** Writing – review & editing, Writing – original draft, Investigation, Conceptualization. **Ping Chen:** Supervision, Resources, Funding acquisition. **Dezhu Liu:** Writing – original draft, Conceptualization. **Yishun Wang:** Writing – review & editing, Formal analysis, Conceptualization. **Linsheng Liu:** Formal analysis, Conceptualization. **Zhenjun Xiao:** Writing – review & editing, Methodology, Investigation. **Zihong Xu:** Writing – review & editing, Methodology. **Yuhang Pan:** Methodology, Investigation, Formal analysis. **Wenying Lv:** Supervision, Resources, Project administration, Funding acquisition, Conceptualization. **Guoguang Liu:** Supervision, Resources, Funding acquisition.

Statement

During the preparation of this work, we used ChatGPT in order to draft this paper for grammar and language refinement. After using this tool, we reviewed and edited the content as needed and take full responsibility for the content of the published article.

Declaration of competing interest

The authors declare that they have no known competing financial interests or personal relationships that could have appeared to influence the work reported in this paper.

Acknowledgments

This work was supported by the National Natural Science Foundation of China [grant numbers 22176042, 21906029, and 22076029]. We would like to thank the Analysis and Test Center of Guangdong University of technology for its help in the relevant instrument analysis.

Appendix A. Supplementary data

Supplementary data to this article can be found online at https://doi.org/10.1016/j.envpol.2024.125598.

Data availability

Data will be made available on request.

References

Boccalon, E., Gorrasi, G., Nocchetti, M., 2020. Layered double hydroxides are still out in the bloom: syntheses, applications and advantages of three-dimensional flower-like structures. Adv. Colloid Interface Sci. 285, 102284. https://doi.org/10.1016/j.cis.2020.102284.

Bokare, A.D., Choi, W., 2015. Singlet-oxygen generation in alkaline periodate solution. Environ. Sci. Technol. 49, 14392–14400. https://doi.org/10.1021/acs.est.5b04119.

Boyd, G.R., Palmeri, J.M., Zhang, S., Grimm, D.A., 2004. Pharmaceuticals and personal care products (PPCPs) and endocrine disrupting chemicals (EDCs) in stormwater canals and Bayou St. John in New Orleans, Louisiana, USA. Sci. Total Environ. 333, 137–148. https://doi.org/10.1016/j.scitotenv.2004.03.018.

Cao, Y., Li, J., Wang, Z., Guan, C., Jiang, J., 2024. The synergistic effect of oxidant-peroxide coupling systems for water and wastewater treatments. Water Res. 249, 120992. https://doi.org/10.1016/j.watres.2023.120992.

Carballa, M., Omil, F., Lema, J.M., Llompart, M.a., Garcıa-Jares, C., Rodrıguez, I., Gómez, M., Ternes, T., 2004. Behavior of pharmaceuticals, cosmetics and hormones in a sewage treatment plant. Water Res. 38, 2918–2926. https://doi.org/10.1016/j.watres.2004.03.029.

Chen, H., Gao, J., Wang, Q., Liu, Y., Fu, X., Guo, Y., Wang, H., Wang, Y., An, J., 2024a. Natural pyrite and ascorbic acid co-enhance periodate activation for inactivation of antibiotic resistant bacteria and inhibition of resistance genes transmission: a green disinfection process dominated by singlet oxygen. J. Hazard Mater. 477, 135217. https://doi.org/10.1016/j.jhazmat.2024.135217.

Chen, H., Yu, Z., Sun, W., Li, T., Zhang, J., Qiu, Z., Younas, M., 2024b. Degradation of Tetracycline through peroxymonosulfate activation with Co/Fe-LDH modified magnetic hydrochar: synergistic effect and low toxicity. Separ. Purif. Technol. 351, 128023. https://doi.org/10.1016/j.seppur.2024.128023.

Chen, L., Huang, H., Zhang, X., Tang, W., He, J., Yang, Y., 2024c. ZIF-67/melamine-derived cobalt encapsulated in N-doped CNTs for periodate activation toward tetracycline degradation. J. Water Proc. Eng. 65, 105879. https://doi.org/10.1016/j.jwpe.2024.105879.

Chen, W., Tian, Y., Liu, D., Yi, Y., Li, X., Wang, J., Bin, L., Li, P., Tang, B., Li, L., 2024d. Unveiling the mechanism of enhanced water purification by F-Fe-Zn-MCM-41 in O_3/PMS. Appl. Catal., B: Environment and Energy 345, 123608. https://doi.org/10.1016/j.apcatb.2023.123608.

Cheng, S., Wu, B., Pang, Y., Shen, X., 2024. Highly efficient heterogeneous electro-Fenton reaction for tetracycline degradation by Fe–Ni LDH@ZIF-67 modified carbon cloth cathode: mechanism and toxicity assessment. J. Environ. Manag. 354, 120336. https://doi.org/10.1016/j.jenvman.2024.120336.

Chia, L.-H., Tang, X., Weavers, L.K., 2004. Kinetics and mechanism of photoactivated periodate reaction with 4-chlorophenol in acidic solution. Environ. Sci. Technol. 38, 6875–6880. https://doi.org/10.1021/es049155n.

Choi, Y., Yoon, H.-I., Lee, C., Vetráková, L.u., Heger, D., Kim, K., Kim, J., 2018. Activation of periodate by freezing for the degradation of aqueous organic pollutants. Environ. Sci. Technol. 52, 5378–5385. https://doi.org/10.1021/acs.est.8b00281.

Deng, J., Ge, Y., Tan, C., Wang, H., Li, Q., Zhou, S., Zhang, K., 2017. Degradation of ciprofloxacin using α-MnO_2 activated peroxymonosulfate process: effect of water constituents, degradation intermediates and toxicity evaluation. Chem. Eng. J. 330, 1390–1400. https://doi.org/10.1016/j.cej.2017.07.137.

Di, X., Zeng, X., Tang, T., Liu, D., Shi, Y., Wang, W., Liu, Z., Jin, L., Ji, X., Shao, X., 2024. Non-radical activation of peroxymonosulfate by modified activated carbon for efficient degradation of oxytetracycline: mechanisms and applications. Separ. Purif. Technol. 349, 127877. https://doi.org/10.1016/j.seppur.2024.127877.

Du, J., Tang, S., Faheem, Ling, H., Zheng, H., Xiao, G., Luo, L., Bao, J., 2019. Insights into periodate oxidation of bisphenol A mediated by manganese. Chem. Eng. J. 369, 1034–1039. https://doi.org/10.1016/j.cej.2019.03.158.

Du, J., Xiao, G., Xi, Y., Zhu, X., Su, F., Kim, S.H., 2020. Periodate activation with manganese oxides for sulfanilamide degradation. Water Res. 169, 115278. https://doi.org/10.1016/j.watres.2019.115278.

Duan, X., O'Donnell, K., Sun, H., Wang, Y., Wang, S., 2015. Sulfur and nitrogen Co-doped graphene for metal-free catalytic oxidation reactions. Small 11, 3036–3044. https://doi.org/10.1002/smll.201403715.

Fang, G., Li, J., Zhang, C., Qin, F., Luo, H., Huang, C., Qin, D., Ouyang, Z., 2022. Periodate activated by manganese oxide/biochar composites for antibiotic degradation in aqueous system: combined effects of active manganese species and biochar. Environ. Pollut. 300, 118939. https://doi.org/10.1016/j.envpol.2022.118939.

Fu, H., Zhang, A., Jin, F., Guo, H., Liu, J., 2022. Ternary NiCeCo-layered double hydroxides grown on $CuBr_2$@ZIF-67 nanowire arrays for high-performance supercapacitors. ACS Appl. Mater. Interfaces 14, 16165–16177. https://doi.org/10.1021/acsami.1c24512.

Fukui, K., 1970. Theory of orientation and stereoselection. In: Fukui, K. (Ed.), Orientation and Stereoselection. Springer, Berlin Heidelberg, Berlin, Heidelberg, pp. 1–85.

Gao, L., Guo, Y., Zhan, J., Yu, G., Wang, Y., 2022. Assessment of the validity of the quenching method for evaluating the role of reactive species in pollutant abatement during the persulfate-based process. Water Res. 221, 118730. https://doi.org/10.1016/j.watres.2022.118730.

Gong, J., Jiang, H., Li, X., Cheng, H., Wang, Z., Cai, J., Li, M., Wang, P., Wang, H., Hu, X., Hu, X., 2024. Highly efficient activation of periodate by a manganese-modified biochar to rapidly degrade methylene blue. Environ. Res. 241, 117657. https://doi.org/10.1016/j.envres.2023.117657.

Gong, Y., Shen, J., Wu, Y., Shen, L., Zhao, S., Zhou, Y., Li, Y., Cui, L., Kang, J., Chen, Z., 2023. Ligands-triggered evolution of catalytic intermediates during periodate activation via soluble Mn(II) for organic contaminants' abatement. Appl. Catal. B Environ. 322, 122093. https://doi.org/10.1016/j.apcatb.2022.122093.

Grimme, S., Antony, J., Ehrlich, S., Krieg, H., 2010. A consistent and accurate ab initio parametrization of density functional dispersion correction (DFT-D) for the 94 elements H-Pu. J. Chem. Phys. 132. https://doi.org/10.1063/1.3382344.

Grimme, S., Ehrlich, S., Goerigk, L., 2011. Effect of the damping function in dispersion corrected density functional theory 32, 1456–1465. https://doi.org/10.1002/jcc.21759.

Guo, W., Dun, C., Yu, C., Song, X., Yang, F., Kuang, W., Xie, Y., Li, S., Wang, Z., Yu, J., Fu, G., Guo, J., Marcus, M.A., Urban, J.J., Zhang, Q., Qiu, J., 2022. Mismatching integration-enabled strains and defects engineering in LDH microstructure for high-rate and long-life charge storage. Nat. Commun. 13, 1409. https://doi.org/10.1038/s41467-022-28918-0.

Guo, Y., Yan, L., Li, X., Yan, T., Song, W., Hou, T., Tong, C., Mu, J., Xu, M., 2021. Goethite/biochar-activated peroxymonosulfate enhances tetracycline degradation: inherent roles of radical and non-radical processes. Sci. Total Environ. 783, 147102. https://doi.org/10.1016/j.scitotenv.2021.147102.

Han, S., Xiao, P., 2022. Catalytic degradation of tetracycline using peroxymonosulfate activated by cobalt and iron co-loaded pomelo peel biochar nanocomposite: characterization, performance and reaction mechanism. Separ. Purif. Technol. 287, 120533. https://doi.org/10.1016/j.seppur.2022.120533.

Han, X., Zhang, W., Li, S., Cheng, C., Zhou, L., Jia, Q., Xiu, G., 2022. Efficient activation of peroxymonosulfate by MnS/Fe-MOF hybrid catalyst for sulfadiazine degradation: synergistic effects and mechanism. Separ. Purif. Technol. 287, 120509. https://doi.org/10.1016/j.seppur.2022.120509.

Hariharan, P.C., Pople, J.A., 1973. The influence of polarization functions on molecular orbital hydrogenation energies. Theor. Chim. Acta 28, 213–222. https://doi.org/10.1007/BF00533485.

He, C., Wang, Y., Li, Z., Huang, Y., Liao, Y., Xia, D., Lee, S., 2020. Facet engineered α-MnO_2 for efficient catalytic ozonation of odor CH_3SH: oxygen vacancy-induced active centers and catalytic mechanism. Environ. Sci. Technol. 54, 12771–12783. https://doi.org/10.1021/acs.est.0c05235.

He, L., Lv, L., Pillai, S.C., Wang, H., Xue, J., Ma, Y., Liu, Y., Chen, Y., Wu, L., Zhang, Z., Yang, L., 2021. Efficient degradation of diclofenac sodium by periodate activation using Fe/Cu bimetallic modified sewage sludge biochar/UV system. Sci. Total Environ. 783, 146974. https://doi.org/10.1016/j.scitotenv.2021.146974.

He, L., Yang, C., Ding, J., Lu, M.-Y., Chen, C.-X., Wang, G.-Y., Jiang, J.-Q., Ding, L., Liu, G.-S., Ren, N.-Q., Yang, S.-S., 2022. Fe, N-doped carbonaceous catalyst activating periodate for micropollutant removal: significant role of electron transfer. Appl. Catal. B Environ. 303, 120880. https://doi.org/10.1016/j.apcatb.2021.120880.

He, Y., Qin, H., Wang, Z., Wang, H., Zhu, Y., Zhou, C., Zeng, Y., Li, Y., Xu, P., Zeng, G., 2024. Fe-Mn oxycarbide anchored on N-doped carbon for enhanced Fenton-like catalysis: importance of high-valent metal-oxo species and singlet oxygen. Appl. Catal. B Environ. 340, 123204. https://doi.org/10.1016/j.apcatb.2023.123204.

He, Z., Chen, M., Xu, M., Zhou, Y., Zhang, Y., Hu, G., 2023. $LaCo_{0.5}Ni_{0.5}O_3$ perovskite for efficient sulfafurazole degradation via peroxymonosulfate activation: catalytic mechanism of interfacial structure. Appl. Catal. B Environ. 335, 122883. https://doi.org/10.1016/j.apcatb.2023.122883.

Hong, Y., Zhou, H., Xiong, Z., Liu, Y., Yao, G., Lai, B., 2020. Heterogeneous activation of peroxymonosulfate by CoMgFe-LDO for degradation of carbamazepine: efficiency, mechanism and degradation pathways. Chem. Eng. J. 391, 123604. https://doi.org/10.1016/j.cej.2019.123604.

Hou, L., Li, X., Yang, Q., Chen, F., Wang, S., Ma, Y., Wu, Y., Zhu, X., Huang, X., Wang, D., 2019. Heterogeneous activation of peroxymonosulfate using Mn-Fe layered double hydroxide: performance and mechanism for organic pollutant degradation. Sci. Total Environ. 663, 453–464. https://doi.org/10.1016/j.scitotenv.2019.01.190.

Huang, Y., Xie, Q., Wang, H., Nawaz, M.I., Zhang, H., Song, S., Hu, K., Wu, Q., 2024. Degradation of trimethoprim in the simulated solar light/periodate system: process and mechanism analysis. J. Water Proc. Eng. 57, 104726. https://doi.org/10.1016/j.jwpe.2023.104726.

Jawad, A., Li, Y., Lu, X., Chen, Z., Liu, W., Yin, G., 2015. Controlled leaching with prolonged activity for Co–LDH supported catalyst during treatment of organic dyes

using bicarbonate activation of hydrogen peroxide. J. Hazard Mater. 289, 165–173. https://doi.org/10.1016/j.jhazmat.2015.02.056.
Jiang, L., Li, W., Wang, H., Yang, J., Chen, H., Wang, X., Yuan, X., Wang, H., 2024. Non-radical activation of low additive periodate by carbon-doped boron nitride for acetaminophen degradation: significance of high-potential metastable intermediates. J. Hazard Mater. 469, 133806. https://doi.org/10.1016/j.jhazmat.2024.133806.
Jin, L., You, S., Duan, X., Yao, Y., Yang, J., Liu, Y., 2022. Peroxymonosulfate activation by Fe_3O_4-MnO_2/CNT nanohybrid electroactive filter towards ultrafast micropollutants decontamination: performance and mechanism. J. Hazard Mater. 423, 127111. https://doi.org/10.1016/j.jhazmat.2021.127111.
Kumar, M., Sridharan, S., Sawarkar, A.D., Shakeel, A., Anerao, P., Mannina, G., Sharma, P., Pandey, A., 2023. Current research trends on emerging contaminants pharmaceutical and personal care products (PPCPs): a comprehensive review. Sci. Total Environ. 859, 160031. https://doi.org/10.1016/j.scitotenv.2022.160031.
Kurban, M., Zhang, Y., Wang, Y., Su, Z., Zhou, T., Zhou, C., Xie, C., Li, L., Li, J., Bai, J., Zhou, B., 2024. Chlorine oxide radical: an emerging free radical for denitrification and pollutant degradation. J. Environ. Chem. Eng. 12, 112630. https://doi.org/10.1016/j.jece.2024.112630.
Li, B., Guo, Z., Cui, Y., Feng, Y., Wu, C., Meng, M., 2021a. LDHs-based 3D modular foam with double metal-fluorine interaction for efficiently promoting peroxymonosulfate activation in water pollutant control. Chem. Eng. J. 425, 131541. https://doi.org/10.1016/j.cej.2021.131541.
Li, W., Zhou, D., Jiang, H., Chen, H., Guo, J., Yang, J., Wang, X., Wang, H., Yuan, X., Jiang, L., 2024. MoO_2 co-catalytic Fe^{3+}/periodate for tetracycline degradation: key role of Fe/Mo cycling and high-valent iron (Fe(IV)) generation. Separ. Purif. Technol. 346, 127509. https://doi.org/10.1016/j.seppur.2024.127509.
Li, Z., Wang, F., Zhang, Y., Lai, Y., Fang, Q., Duan, Y., 2021b. Activation of peroxymonosulfate by $CuFe_2O_4$-$CoFe_2O_4$ composite catalyst for efficient bisphenol a degradation: synthesis, catalytic mechanism and products toxicity assessment. Chem. Eng. J. 423, 130093. https://doi.org/10.1016/j.cej.2021.130093.
Lin, Z., Wu, Y., Jin, X., Liang, D., Jin, Y., Huang, S., Wang, Z., Liu, H., Chen, P., Lv, W., Liu, G., 2023. Facile synthesis of direct Z-scheme UiO-66-NH_2/PhC_2Cu heterojunction with ultrahigh redox potential for enhanced photocatalytic Cr(VI) reduction and NOR degradation. J. Hazard Mater. 443, 130195. https://doi.org/10.1016/j.jhazmat.2022.130195.
Lindqvist, N., Tuhkanen, T., Kronberg, L., 2005. Occurrence of acidic pharmaceuticals in raw and treated sewages and in receiving waters. Water Res. 39, 2219–2228. https://doi.org/10.1016/j.watres.2005.04.003.
Ling, C., Wu, S., Han, J., Dong, T., Zhu, C., Li, X., Xu, L., Zhang, Y., Zhou, M., Pan, Y., 2022. Sulfide-modified zero-valent iron activated periodate for sulfadiazine removal: performance and dominant routine of reactive species production. Water Res. 220, 118676. https://doi.org/10.1016/j.watres.2022.118676.
Liu, G., Xie, C., Zhang, Y., Du, Y., Wang, J., Lin, J., Bai, J., Li, J., Zhou, C., Zhou, T., Zhou, B., 2024a. Synergistic etching of nickel foam by Fe^{3+} and Cl^- ions to synthesize nickel-iron-layered double hydroxide nanolayers with abundant oxygen vacancies for superior urea oxidation. J. Colloid Interface Sci. 668, 375–384. https://doi.org/10.1016/j.jcis.2024.04.123.
Liu, J.-L., Wong, M.-H., 2013. Pharmaceuticals and personal care products (PPCPs): a review on environmental contamination in China. Environ. Int. 59, 208–224. https://doi.org/10.1016/j.envint.2013.06.012.
Liu, L., Wang, Y., Zhang, Y., Chen, P., Liu, D., Niu, M., Jian, J., Xu, Z., Zhang, S., Lv, W., Liu, G., 2024b. Enhanced degradation of sulfonamides by copper and cuprous oxides activated ferrate (VI) synergistically: mechanism and applicability. J. Environ. Chem. Eng. 12, 113936. https://doi.org/10.1016/j.jece.2024.113936.
Liu, Y., Luo, J., Tang, L., Feng, C., Wang, J., Deng, Y., Liu, H., Yu, J., Feng, H., Wang, J., 2020. Origin of the enhanced reusability and electron transfer of the carbon-coated Mn_3O_4 nanocube for persulfate activation. ACS Catal. 10, 14857–14870. https://doi.org/10.1021/acscatal.0c04049.
Long, Y., Cao, Z., Wu, W., Liu, W., Yang, P., Zhan, X., Chen, R., Liu, D., Huang, W., 2024. Rational modulation of Fe single-atom electronic structure in a Fe-N_2B_4 configuration for preferential $^1O_2$ generation in Fenton-like reactions. Appl. Catal., B: Environment and Energy 344, 123643. https://doi.org/10.1016/j.apcatb.2023.123643.
Long, Y., Dai, J., Zhao, S., Huang, S., Zhang, Z., 2022. Metal–organic framework-derived magnetic carbon for efficient decontamination of organic pollutants via periodate activation: surface atomic structure and mechanistic considerations. J. Hazard Mater. 424, 126786. https://doi.org/10.1016/j.jhazmat.2021.126786.
Long, Y., Dai, J., Zhao, S., Su, Y., Wang, Z., Zhang, Z., 2021. Atomically dispersed cobalt sites on graphene as efficient periodate activators for selective organic pollutant degradation. Environ. Sci. Technol. 55, 5357–5370. https://doi.org/10.1021/acs.est.0c07794.
Lu, T., Chen, F., 2012. Multiwfn: a multifunctional wavefunction analyzer. J. Comput. Chem. 33, 580–592. https://doi.org/10.1002/jcc.22885.
Lu, T., Chen, Q., 2022. Realization of Conceptual Density Functional Theory and Information-Theoretic Approach in Multiwfn Program, Conceptual Density Functional Theory, pp. 631–647.
Ma, R., Yan, X., Mi, X., Wu, Y., Qian, J., Zhang, Q., Chen, G.-H., 2021. Enhanced catalytic degradation of aqueous doxycycline (DOX) in Mg-Fe-LDH@biochar composite-activated peroxymonosulfate system: performances, degradation pathways, mechanisms and environmental implications. Chem. Eng. J. 425, 131457. https://doi.org/10.1016/j.cej.2021.131457.
Mi, X., Ma, R., Pu, X., Fu, X., Geng, M., Qian, J., 2022. FeNi-layered double hydroxide (LDH)@biochar composite for , activation of peroxymonosulfate (PMS) towards enhanced degradation of doxycycline (DOX): characterizations of the catalysts, catalytic performances,degradation pathways and mechanisms. J. Clean. Prod. 378, 134514. https://doi.org/10.1016/j.jclepro.2022.134514.
Mochizuki, Y., Bud, J., Liu, J., Takahashi, M., Tsubouchi, N., 2021. Adsorption of phosphate from aqueous using iron hydroxides prepared by various methods. J. Environ. Chem. Eng. 9, 104645. https://doi.org/10.1016/j.jece.2020.104645.
Morell, C., Grand, A., Toro-Labbé, A., 2005. New dual descriptor for chemical reactivity. J. Phys. Chem. 109, 205–212. https://doi.org/10.1021/jp046577a.
Naik, S.S., Lee, S.J., Theerthagiri, J., Yu, Y., Choi, M.Y., 2021. Rapid and highly selective electrochemical sensor based on ZnS/Au-decorated f-multi-walled carbon nanotube nanocomposites produced via pulsed laser technique for detection of toxic nitro compounds. J. Hazard Mater. 418, 126269. https://doi.org/10.1016/j.jhazmat.2021.126269.
Ni, J., Wen, Y., Pan, D., Bai, J., Zhou, B., Zhao, S., Wang, Z., Liu, Y., Zeng, Q., 2023. Light-driven simultaneous water purification and green energy production by photocatalytic fuel cell: a comprehensive review on current status, challenges, and perspectives. Chem. Eng. J. 473, 145162. https://doi.org/10.1016/j.cej.2023.145162.
Niu, L., Lin, J., Chen, W., Zhang, Q., Yu, X., Feng, M., 2023. Ferrate(VI)/Periodate system: synergistic and rapid oxidation of micropollutants via periodate/iodate-modulated Fe(IV)/Fe(V) intermediates. Environ. Sci. Technol. 57, 7051–7062. https://doi.org/10.1021/acs.est.2c08965.
Pan, B., Xing, B., 2008. Adsorption mechanisms of organic chemicals on carbon nanotubes. Environ. Sci. Technol. 42, 9005–9013. https://doi.org/10.1021/es801777n.
Qian, J., Ma, R., Chen, Z., Wang, G., Zhang, Y., Du, Y., Chen, Y., An, T., Ni, B.-J., 2023. Hierarchical Co-Fe layered double hydroxides (LDH)/Ni foam composite as a recyclable peroxymonosulfate activator towards monomethylhydrazine degradation: enhanced electron transfer and $^1O_2$ dominated non-radical pathway. Chem. Eng. J. 469, 143554. https://doi.org/10.1016/j.cej.2023.143554.
Rad, T.S., Ansarian, Z., Soltani, R.D.C., Khataee, A., Orooji, Y., Vafaei, F., 2020. Sonophotocatalytic activities of FeCuMg and CrCuMg LDHs: influencing factors, antibacterial effects, and intermediate determination. J. Hazard Mater. 399, 123062. https://doi.org/10.1016/j.jhazmat.2020.123062.
Sadeghi Rad, T., Khataee, A., Arefi-Oskoui, S., Sadeghi Rad, S., Orooji, Y., Gengec, E., Kobya, M., 2022. Graphene-based ZnCr layered double hydroxide nanocomposites as bactericidal agents with high sonophotocatalytic performances for degradation of rifampicin. Chemosphere 286, 131740. https://doi.org/10.1016/j.chemosphere.2021.131740.
Santos, J.L., Aparicio, I., Alonso, E., 2007. Occurrence and risk assessment of pharmaceutically active compounds in wastewater treatment plants. A case study: seville city (Spain). Environ. Int. 33, 596–601. https://doi.org/10.1016/j.envint.2006.09.014.
Saravanan, A., Deivayanai, V.C., Kumar, P.S., Rangasamy, G., Hemavathy, R.V., Harshana, T., Gayathri, N., Alagumalai, K., 2022. A detailed review on advanced oxidation process in treatment of wastewater: mechanism, challenges and future outlook. Chemosphere 308, 136524. https://doi.org/10.1016/j.chemosphere.2022.136524.
Shen, S., Jiang, W., Zhao, Q., He, L., Ma, Y., Zhou, X., Wang, J., Yang, L., Chen, Z., 2023. Molten-salts assisted preparation of iron-nitrogen-carbon catalyst for efficient degradation of acetaminophen by periodate activation. Sci. Total Environ. 859, 160001. https://doi.org/10.1016/j.scitotenv.2022.160001.
Shin, J., von Gunten, U., Reckhow, D.A., Allard, S., Lee, Y., 2018. Reactions of ferrate(VI) with iodide and hypoiodous acid: kinetics, pathways, and implications for the fate of iodine during water treatment. Environ. Sci. Technol. 52, 7458–7467. https://doi.org/10.1021/acs.est.8b01565.
Song, Y., Tian, J., Gao, S., Shao, P., Qi, J., Cui, F., 2017. Photodegradation of sulfonamides by g-C_3N_4 under visible light irradiation: effectiveness, mechanism and pathways. Appl. Catal. B Environ. 210, 88–96. https://doi.org/10.1016/j.apcatb.2017.03.059.
Sun, H., He, F., Choi, W., 2020. Production of reactive oxygen species by the reaction of periodate and hydroxylamine for rapid removal of organic pollutants and waterborne bacteria. Environ. Sci. Technol. 54, 6427–6437. https://doi.org/10.1021/acs.est.0c00817.
Theerthagiri, J., Karuppasamy, K., Lee, S.J., Shwetharani, R., Kim, H.-S., Pasha, S.K.K., Ashokkumar, M., Choi, M.Y., 2022a. Fundamentals and comprehensive insights on pulsed laser synthesis of advanced materials for diverse photo- and electrocatalytic applications. Light Sci. Appl. 11, 250. https://doi.org/10.1038/s41377-022-00904-7.
Theerthagiri, J., Lee, Seung J., Karuppasamy, K., Arulmani, S., Veeralakshmi, S., Ashokkumar, M., Choi, M.Y., 2021. Application of advanced materials in sonophotocatalytic processes for the remediation of environmental pollutants. J. Hazard Mater. 412, 125245. https://doi.org/10.1016/j.jhazmat.2021.125245.
Theerthagiri, J., Park, J., Das, H.T., Rahamathulla, N., Cardoso, E.S.F., Murthy, A.P., Maia, G., Vo, D.V.N., Choi, M.Y., 2022b. Electrocatalytic conversion of nitrate waste into ammonia: a review. Environ. Chem. Lett. 20, 2929–2949. https://doi.org/10.1007/s10311-022-01469-y.
Wang, G., Huang, D., Cheng, M., Du, L., Huang, H., Li, R., Xu, W., Li, S., Zhou, W., Ren, Y., 2024a. Lamellar cluster-like grown FeCo layered double hydroxides as stable peroxymonosulfate activators at wide circumneutral pH. Chem. Eng. J. 488, 150692. https://doi.org/10.1016/j.cej.2024.150692.
Wang, N., Kang, G., Hu, G., Chen, J., Qi, D., Bi, F., Chang, N., Gao, Z., Zhang, S., Shen, W., 2023. Spatiotemporal distribution and ecological risk assessment of pharmaceuticals and personal care products (PPCPs) from Luoma Lake, an important node of the South-to-North Water Diversion Project. Environ. Monit. Assess. 195, 1330. https://doi.org/10.1007/s10661-023-11976-2.
Wang, X., Huang, H., Li, W., Chen, H., Liu, W., Yang, J., Yuan, X., Wang, H., Chen, Y., Jiang, L., 2024b. Ultra-thin carbon nitride activated periodate for efficient

tetracycline degradation with the assistance of visible light. Separ. Purif. Technol. 338, 126505. https://doi.org/10.1016/j.seppur.2024.126505.

Wang, Y., Zhang, L., Qiu, Z., Ren, X., Song, J., Gao, D., Guo, Q., Wang, L., Hu, X., 2024c. Facile preparation of AlCo-LDH/sepiolite composites as peroxymonosulfate catalysts for efficient degradation of norfloxacin: performance, reaction mechanism and degradation pathway. J. Environ. Chem. Eng. 12, 112231. https://doi.org/10.1016/j.jece.2024.112231.

Wang, Z., Srivastava, V., Wang, S., Sun, H., Thangaraj, S.K., Jänis, J., Sillanpää, M., 2020. UVC-assisted photocatalytic degradation of carbamazepine by Nd-doped Sb_2O_3/TiO_2 photocatalyst. J. Colloid Interface Sci. 562, 461–469. https://doi.org/10.1016/j.jcis.2019.11.094.

Xiong, M., Yan, J., Fan, G., Liu, Y., Chai, B., Wang, C., Song, G., 2022. Built-in electric field mediated peroxymonosulfate activation over biochar supported-Co_3O_4 catalyst for tetracycline hydrochloride degradation. Chem. Eng. J. 444, 136589. https://doi.org/10.1016/j.cej.2022.136589.

Xu, M., Yang, J., Wang, Y., Lu, B., Chen, R., Liu, H., 2022. Novel urchin-like Co_5Mn-LDH hierarchical nanoarrays: formation mechanism and its performance in PMS activation and norfloxacin degradation. Separ. Purif. Technol. 300, 121822. https://doi.org/10.1016/j.seppur.2022.121822.

Xu, W., Zheng, X., Shangguan, Z., Qu, J., Zhang, W., 2023. A low-cost magnetic catalyst ($MnFe_2O_4$) for ciprofloxacin degradation via periodate activation: the synergistic effect of Mn and Fe. Chem. Eng. J. 464, 142562. https://doi.org/10.1016/j.cej.2023.142562.

Yan, J., Zhang, X., Zheng, W., Lee, L.Y.S., 2021. Interface engineering of a 2D-C_3N_4/NiFe-LDH heterostructure for highly efficient photocatalytic hydrogen evolution. ACS Appl. Mater. Interfaces 13, 24723–24733. https://doi.org/10.1021/acsami.1c03240.

Yang, Y., Wu, Y., Guo, D., Liu, L., 2024a. Effect of fluorine content in layered double hydroxide catalyzing oxygen evolution. Appl. Surf. Sci. 644, 158810. https://doi.org/10.1016/j.apsusc.2023.158810.

Yang, Z., Yang, k., Zhang, C., 2024b. Defect-engineered Ni-Fe-LDH with porous flower-like architecture enables boosted advanced oxidation processes: experimental and theoretical studies. Separ. Purif. Technol. 333, 125885. https://doi.org/10.1016/j.seppur.2023.125885.

Yao, J., Zeng, X., Wang, Z., 2017. Enhanced degradation performance of sulfisoxazole using peroxymonosulfate activated by copper-cobalt oxides in aqueous solution: kinetic study and products identification. Chem. Eng. J. 330, 345–354. https://doi.org/10.1016/j.cej.2017.07.155.

Yeon, S., Lee, S.J., Kim, J., Begildayeva, T., Min, A., Theerthagiri, J., Kumari, M.L.A., Pinto, L.M.C., Kong, H., Choi, M.Y., 2022. Sustainable removal of nitrite waste to value-added ammonia on Cu@Cu_2O core–shell nanostructures by pulsed laser technique. Environ. Res. 215, 114154. https://doi.org/10.1016/j.envres.2022.114154.

Yu, J., Qiu, W., Lin, X., Wang, Y., Lu, X., Yu, Y., Gu, H., Heng, S., Zhang, H., Ma, J., 2023. Periodate activation with stable $MgMn_2O_4$ spinel for bisphenol A removal: radical and non-radical pathways. Chem. Eng. J. 459, 141574. https://doi.org/10.1016/j.cej.2023.141574.

Yu, Y., Min, A., Jung, H.J., Theerthagiri, J., Lee, S.J., Kwon, K.-Y., Choi, M.Y., 2021. Method development and mechanistic study on direct pulsed laser irradiation process for highly effective dechlorination of persistent organic pollutants. Environ. Pollut. 291, 118158. https://doi.org/10.1016/j.envpol.2021.118158.

Zeng, H., Chen, Y., Xu, J., Li, S., Wu, J., Li, D., Zhang, J., 2024. Iron-based materials for activation of periodate in water and wastewater treatment processes: the important role of Fe species. Chem. Eng. J. 482, 148885. https://doi.org/10.1016/j.cej.2024.148885.

Zhang, C., Tian, S., Qin, F., Yu, Y., Huang, D., Duan, A., Zhou, C., Yang, Y., Wang, W., Zhou, Y., Luo, H., 2021. Catalyst-free activation of permanganate under visible light irradiation for sulfamethazine degradation: experiments and theoretical calculation. Water Res. 194, 116915. https://doi.org/10.1016/j.watres.2021.116915.

Zhang, K., Zhang, S., Ye, C., Ou, R., Zeng, H., Yu, X., Feng, M., 2023. Sunlight-activated periodate oxidation: a novel and versatile strategy for highly efficient water decontamination. Chem. Eng. J. 451, 138642. https://doi.org/10.1016/j.cej.2022.138642.

Zhang, N., Zhang, B., Wang, C., Sui, H., Zhang, N., Wen, Z., He, A., Zhang, R., Xue, R., 2024. Magnetic CoFe hydrotalcite composite Co metal–organic framework material efficiently activating peroxymonosulfate to degrade sulfamethoxazole: oxygen vacancy-mediated radical and non-radical pathways. J. Colloid Interface Sci. 671, 110–123. https://doi.org/10.1016/j.jcis.2024.05.166.

Zheng, X., Xu, T., Kang, X., Xing, Y., Cao, Y., Gui, X., 2022. Structural dependent persulfate activation by coke powder for aniline degradation. Chem. Eng. J. 431, 134088. https://doi.org/10.1016/j.cej.2021.134088.

Zhu, L., Ji, J., Liu, J., Mine, S., Matsuoka, M., Zhang, J., Xing, M., 2020. Designing 3D-MoS_2 sponge as excellent cocatalysts in advanced oxidation processes for pollutant control. Angew. Chem. Int. Ed. 59, 13968–13976. https://doi.org/10.1002/anie.202006059.

Zong, Y., Shao, Y., Zeng, Y., Shao, B., Xu, L., Zhao, Z., Liu, W., Wu, D., 2021. Enhanced oxidation of organic contaminants by iron(II)-Activated periodate: the significance of high-valent iron–oxo species. Environ. Sci. Technol. 55, 7634–7642. https://doi.org/10.1021/acs.est.1c00375.